

Article

Pervasive Listwaenitization: The Role of Subducted Sediments within Mantle Wedge, W. Chalkidiki Ophiolites, N. Greece

Alkiviadis Sideridis ^{1,*}, Petros Koutsovitis ¹, Basilios Tsikouras ², Christos Karkalis ³,
Christoph Hauzenberger ⁴, Federica Zaccarini ², Pavlos Tsitsanis ⁵, Christina Vasiliki Lazaratou ¹, Vasilios Skliros ⁶,
Dionisios Panagiotaras ⁷, Dimitrios Papoulis ¹ and Konstantin Hatzipanagiotou ¹

¹ Section of Earth Materials, Department of Geology, University of Patras, 26504 Patras, Greece

² Geosciences Programme, Faculty of Science, Universiti Brunei Darussalam, Gadong BE1410, Brunei

³ Faculty of Geology and Geoenvironment, National and Kapodistrian University of Athens, Panepistimioupoli Zografou, 15784 Athens, Greece

⁴ NAWI Graz Geocenter, University of Graz, Universitätsplatz 2, 8010 Graz, Austria

⁵ Independent Researcher, Makedonias 21, 63200 Nea Moudania, Greece

⁶ School of Mining and Metallurgical Engineering, National Technical University of Athens, 15773 Athens, Greece

⁷ Department of Environment, Ionian University, 29100 Zakynthos, Greece

* Correspondence: a.sideridis@upnet.gr



Citation: Sideridis, A.; Koutsovitis, P.; Tsikouras, B.; Karkalis, C.; Hauzenberger, C.; Zaccarini, F.; Tsitsanis, P.; Lazaratou, C.V.; Skliros, V.; Panagiotaras, D.; et al. Pervasive Listwaenitization: The Role of Subducted Sediments within Mantle Wedge, W. Chalkidiki Ophiolites, N. Greece. *Minerals* **2022**, *12*, 1000. <https://doi.org/10.3390/min12081000>

Academic Editors: Jingsui Yang, Souvik Das and Weiwei Wu

Received: 22 June 2022

Accepted: 6 August 2022

Published: 8 August 2022

Publisher's Note: MDPI stays neutral with regard to jurisdictional claims in published maps and institutional affiliations.



Copyright: © 2022 by the authors. Licensee MDPI, Basel, Switzerland. This article is an open access article distributed under the terms and conditions of the Creative Commons Attribution (CC BY) license (<https://creativecommons.org/licenses/by/4.0/>).

Abstract: Listwaenitization processes have significantly altered the mantle section of the West Chalkidiki ophiolites, generating the second largest magnesite deposit in Greece. Although research studies have been conducted in the region, the post-magmatic processes, and especially the geotectonic settings under which listwaenitization took place, remain unclear. In this study, minerals and rocks were studied applying XRD, clay fraction, SEM, EMPA, ICP-MS, INAA, LA-ICP-MS, and thermodynamic modeling. The results revealed that alteration processes significantly affected the mantle wedge peridotite protoliths leading to the following chemical changes (a) SiO₂ increase with decreasing MgO, (b) Cs, Pb, As, and V enrichments, (c) limited alteration of magnesiochromite hosted within listwaenitized chromitites and (d) enrichment in PPGE and Au in listwaenitized chromitites and desulfurized laurite. Alteration was induced by fluids deriving from subducted Mesozoic sediments, represented by the Prinochori Formation or chemically similar formations. The final product of completely silicified peridotite (silica listwaenite) is thermodynamically stable in Earth-surface conditions, with dolomite and phyllosilicates transforming into clay minerals. Based on detailed petrographical observations, peridotites were subjected to serpentinization, and subsequently, serpentine interacted with CO₂, silica and calcium-bearing fluids, leading to its transformation into amorphous rusty-silica mass and/or tremolite.

Keywords: listwaenite; chromitite; platinum-group minerals; platinum-group elements; Perple_X pseudosections; magnesite; Gerakini-Ormylia; Vavdos

1. Introduction

Listwaenites are commonly formed at fore-arc environments above subduction zones, which are comprised of highly altered mantle rocks, with their primary minerals having been replaced by carbonates and secondary silicates [1–4]. Local deformation greatly affects and controls their formation [5,6]. In extreme cases, primary minerals can be completely replaced by silica [3,5], giving rise to silica listwaenites/birbirites/quartzites [3,4,7]. These changes are the aftermath of fluid-rock interaction at low pressure and temperatures < 300 °C [8], with the metasomatic fluids considered to be enriched in CO₂ [3,9,10]. The source of the CO₂ is still uncertain [11], with research pointing to either (a) meteoric [12] or (b) hypogene processes [13]. The Greek listwaenites of the Chalkidiki peninsula and Euboea Island are considered to have been formed after the interaction of meteoric-related fluids with an

organic carbon input (mainly based upon C and O isotopes of magnesite) [14], however, research concerning the source of carbon has been limited to the use of magnesite isotopic compositions. Trace element chemistry of whole-rock listwaenitized samples, as well as of their secondary mineral phases, are oftentimes not considered when models for the formation of listwaenites are proposed. Additionally, listwaenites are favored gold exploration targets, since enrichment in Au is a rather common feature [15].

Chromitites are a major component of ophiolites' mantle sections and they oftentimes undergo post-magmatic processes altering their primary composition [1,16–18]. To our knowledge, the effect of listwaenitization upon chromitites and their minerals has not been a subject of extensive scientific research. Since chromitites are excellent tools to study magmatic and post-magmatic processes, the effects of listwaenitization on chromitites should be established.

Subducted sediments hold great significance concerning processes that take effect within the earth's mantle, and more precisely, the mantle wedge [19]. These processes include a variety of metasomatism types, e.g., rodingitization, listwaenitization, and serpentinization [19], as well as genesis of newly formed rocks after anatexis, expressed as granitic intrusions [20,21]. Although research exists concerning the participation of fluids deriving from subducted sediments [4,8], most often this sedimentary source is not correlated with field geology and actual sedimentary outcrops.

In the present study, the geological settings under which the W. Chalkidiki listwaenites were formed are being reported for the first time. Chromitites are used to test their degree and type of modification under listwaenitization conditions. New datasets focused on trace mineral and whole-rock geochemistry are being presented, offering a comprehensive view on the alteration processes, modeling the conditions of the serpentinization-to-listwaenitization transition. In addition, this study also attempts to locate the source of the CO₂-bearing fluids that induced listwaenitization.

2. Geological Settings

The Vavdos and Gerakini-Ormylia neighboring ophiolites are part of the West Chalkidiki dismembered ophiolite complex. Together with the dismembered ophiolite units of Guevgueli, Thessaloniki/Oreokastro, and South Chalkidiki (Innermost Vardar Zone ophiolites), they crop-out along the contact of the Circum-Rhodope Belt (CRB) and Vardar Zone (VZ), and they originate from the Vardar Ocean Figure 1a; [22,23]). The CRB, in the area of Chalkidiki, is segregated into the Examili, Pirgoto, Melissochori, and Chortiatis formations and the Aspri Vrissi Series [24,25]. CRB consists of Mesozoic sedimentary rocks, arc-derived igneous rocks, and metamorphic rocks [24,25]. Another sedimentary formation adjacent to the ophiolites of West Chalkidiki is the Princhori formation, consisting of low-Ca psammitic rocks [26], which outcrops within the Vardar zone, south-west from the ophiolites. It dates from the early Cretaceous and it was deposited in proximity with the Vardar ophiolitic rocks; its detrital spinel grains point to both MOR (middle ocean ridge) and SSZ (supra subduction zone) peridotite sources [26].

In general, the studied occurrences are comprised by similar formations (a) a significant SSZ-derived mantle portion consisting of harzburgite and dunite that hosts podiform chromitite, (b) crustal ultramafic cumulates (wherlite, websterite, clinopyroxenite) along the mantle-Moho transition, (c) crustal mafic cumulates consisting of various gabbroic lithologies, and (d) granitic pegmatites (Figure 1b,c, Vavdos and Gerakini-Ormylia ophiolites, respectively). Both mantle sections, occurring in Vavdos and Gerakini-Ormylia, had undergone the same processes that led to the genesis of the chromitite occurrences after high partial melting degrees in a SSZ fore-arc environment, hence, the great chemical similarities in mineral chemistry, PGE contents, and geochemistry [22,27]. The NW-SE trending ophiolites of Vavdos and Gerakini-Ormylia are bounded by the arc-related magmatic Chortiatis suite. Massive diorite originating from this arc formation crops out NE from the Gerakini-Ormylia ophiolite [28]. The ophiolites are overthrust upon the Serbomacedonian Massif (SM) metamorphic basement. The mantle section is variably serpentinized and

carbonized; listwaenitization is limited within the mantle section. The magnesite ore veins and stockwork penetrate mainly within dunites regardless of their alteration degree.

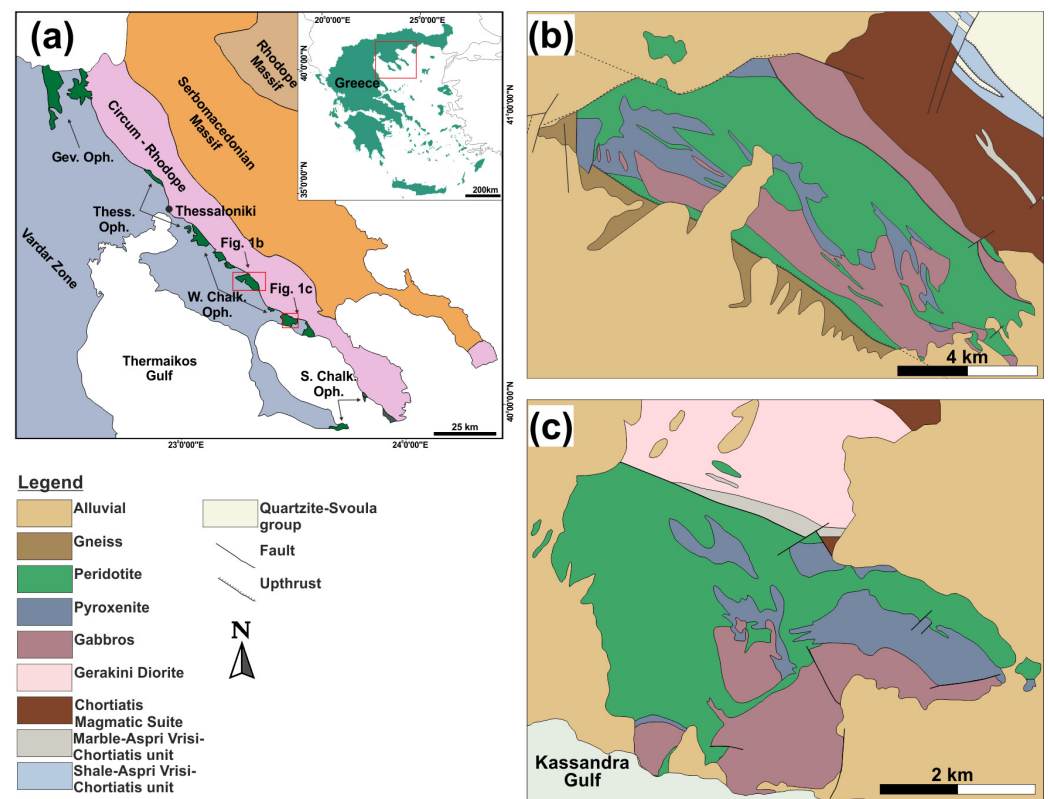


Figure 1. (a) Innermost Vardar Zone ophiolites: Geuvveli complex (Gev. Oph.), Thessaloniki ophiolites (Thess. Oph.), West Chalkidiki ophiolites (W. Chalk. Oph.) and South Chalkidiki ophiolites (S. Chalk. Oph.); (b) Vavdos ophiolite; (c) Gerakini-Ormylia ophiolite. (b,c) are modified after Poliyiros and Arnaia sheets of the Hellenic Survey of Geology and Mineral Exploration (HSGME).

3. Materials and Methods

The studied samples were collected from the ophiolites of Vavdos and Gerakini-Ormylia (Table S1). Electron microprobe analyses of chromite, chlorite, and tremolite were conducted at the Eugen F. Stumpfl Laboratory of the Leoben University, Austria, using a Superprobe Jeol JXA 8200 instrument (JEOL, Tokyo, Japan). The analytical conditions are described by [22]. Whole-rock analyses as well as PGE geochemical analyses were conducted in Actlabs, Canada, using the packages 4Lithores and 1B1-Fire Assay-INAA, respectively. Trace element contents in tremolite were determined on polished thin sections and blocks by the LA-ICP-MS system at the NAWI Graz Central Lab for Water, Minerals and Rocks (University of Graz (Graz, Austria) and Graz University of Technology (Graz, Austria)), with an ESI New Wave 193 Excimer Laser (193 nm wavelength) coupled to a quadrupole Agilent 7500 CX mass spectrometer. A beam size of 50 μm , with a fluence of $\sim 5 \text{ J/cm}^2$, helium flow of 0.8 L/min, 25 s gas blank followed by 50 s of ablation and a dwell time of 20 s for each mass were used for the element analyses. The reference material NIST SRM 612 was used for standardization, and Si and Al as internal calibration elements for tremolite and magnesiochromite, respectively. The USGS reference glass BCR-2G was analyzed as monitor standard, which could be reproduced within errors. For data reduction, the software “GLITTER” was used and the values for NIST SRM 612 were taken from [29]. Samples enriched in clay minerals were dried at 45 °C and sieved until powdered diffraction was obtained. The finest sedimentations of $\leq 2 \mu\text{m}$ were separated using the clay fraction method [30] in order to be characterized via XRD technique. X-ray diffraction (XRD) patterns were obtained for the samples in a 2θ range of 2° to 60° and at a scanning rate of 2°/min using an XRD Bruker D8 advance diffractometer with Ni-filtered

CuK α radiation ($\lambda = 1.5418 \text{ \AA}$) (Geology Department, University of Patras, Patras, Greece). The morphological characteristics of each sample were verified with scanning electron microscopy (SEM) using a SEM LEO SUPRA 35VP, situated at the FORTH/ICE-HT, Patras. Petrographical evaluation through Quantitative Evaluation of Minerals by Scanning Electron Microscopy (QEMSCAN) is described by [23].

4. Results

4.1. Field Geology and Petrography

Listwaenitization is solely confined within the mantle section of the studied ophiolites (Figure 2a); magnesite veins cross-cutting the ultramafic cumulates are rather rare. Dark-colored serpentinites were noticed occupying 2-m-thick fault zones and they do not appear as massive extended bodies (Figure 2b). Massive cryptocrystalline magnesite veins are accompanied by dolomite, calcite, opal, and quartz, reaching up to 1.5 m in thickness (Figure 2c). Tremolite, chlorite, serpentine, and quartz were encountered within the magnesite veins. Opal is found in occurrences in proximity with highly serpentinized dunite. Magnesite \pm dolomite veins cross-cut variably metasomatized mantle peridotites (mainly dunite) ranging from fresh to serpentinized and completely silicified (complete listwaenitization). Magnesite also occurs as disseminated concentrations. Dolomite concentrations are elevated towards the higher stratigraphical levels. Listwaenites do not necessarily host the magnesite ore (Figure 2d). Oftentimes, around the vein rims, a thin serpentine-chlorite-tremolite alteration front is developed. Since podiform chromitites are hosted within the dunite bodies, they have also experienced listwaenitization and deposition of carbonate and silicate minerals (Figure 2e). Chromitites appear with massive, banded, and schlieren textures. Peculiar textured nodular dolomite-quartz-biotite veins along with tremolite veins cross-cut altered listwaenite (Figure 2f). Rims of chlorite and clay minerals are developed laterally from the aforementioned vein. The clay minerals are represented by smectite and fibrous varieties (sepiolite and palygorskite). Both XRD (Figure 3a) and morphological characterization via SEM (Figure 3b–d) confirms this grouping. Smectite is transformed into fibrous clay minerals (Figure 3b). Tightened growth of palygorskite fibers took place upon phyllosilicate minerals (Figure 3c), whereas sepiolite covers dolomite surfaces (Figure 3d). Sepiolite fibers are typically $\sim 42 \text{ nm}$ wide. In Vavdos ophiolite, a limited talc schist zone has been identified at the contact of the listwaenitized mantle section with the Serbomacedonian Massif's gneisses.

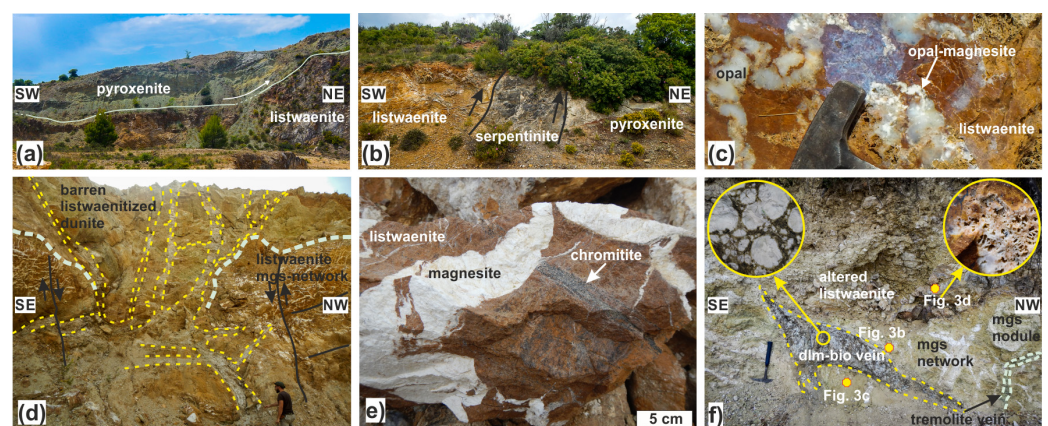


Figure 2. Selective field photos (a) contact between unaltered massive pyroxenite and listwaenite with magnesite stockwork; (b) fault-zone serpentinite body developed between the contact of listwaenite and pyroxenite (c) listwaenite cross-cut by opal and magnesite; (d) barren listwaenite overlying magnesite bearing listwaenite, whitish veins are composed of dolomite-chlorite; (e) listwaenite hosting both chromite and magnesite ore (f) vein consisting of nodular dolomite and biotite cross-cutting altered listwaenite, Figure 3b–d (black dots represent where the samples were collected) stand for the XRD patterns presented in Figure 3. Abbreviations: mgs = magnesite.

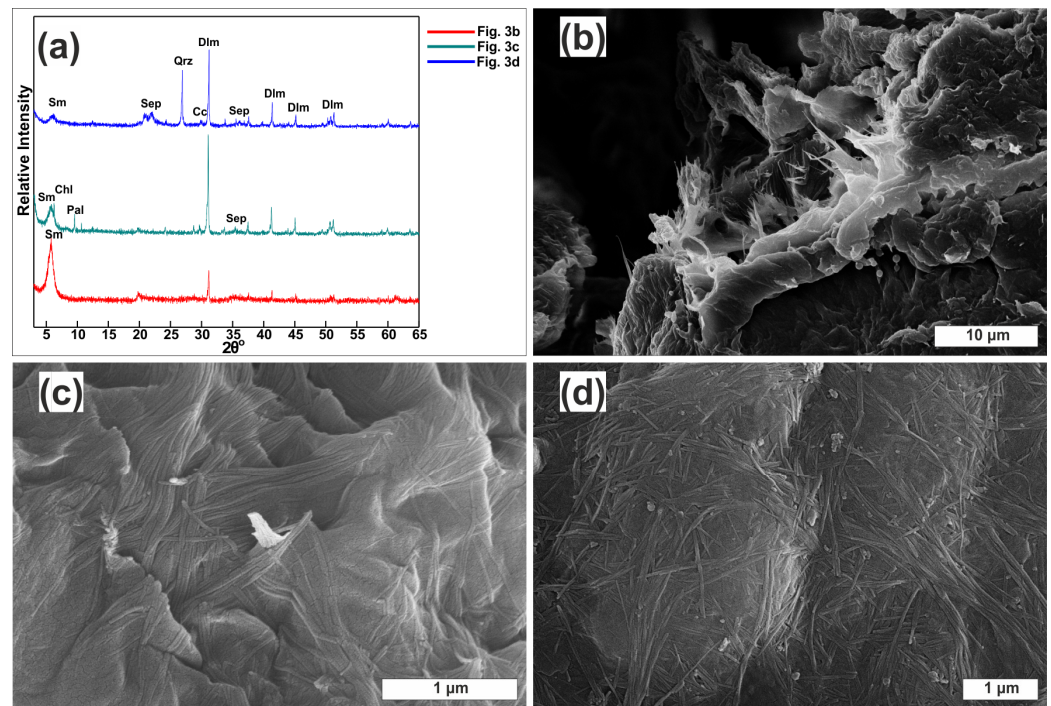


Figure 3. (a) XRD patterns of the samples referred in Figure 2f; (b) typical layered smectite structure altering into fibrous clay minerals within completely altered peridotite; (c) palygorskite fibers covering phyllosilicate minerals within completely altered green-colored peridotite; (d) typical fibrous morphology of sepiolite within vuggy listwaenite. Abbreviations: Sm = smectite; Sep = sepiolite; Cc = calcite; Dlm = dolomite; Chl = chlorite; Pal = palygorskite.

During the initial stages of dunite alteration, olivine is altered into serpentine and beige-colored dolomite (Figure 4a), whereas orthopyroxene is transformed into talc and magnesite. These processes lead to the diminishing concentrations of olivine and its simultaneous size reduction (from 800 to 86 μm ; Figure 4a–c). The dunite texture is cataclastic, and in places, mylonitic (Figure 4b). The end product of this alteration is an iddingsitized serpentinized dunite (proto-listwaenite). In places where fluid circulation was more prominent, the serpentinized dunites underwent silicification (Figure 4d). Listwaenites (true listwaenite) are the typical hosts of magnesite ore. Listwaenites host variable concentrations of magnesite ore and its accompanying minerals. The microcrystalline silica mass is red-colored (rusty silica), and in places, it has been recrystallized into quartz. During petrographic study, lithotypes consisting of both rusty silica mass and serpentine were identified. The rusty silica pseudomorphically retains serpentine’s mesh texture (Figure 4d). Another silicate mineral phase that is found both in magnesite veins and listwaenitized chromitite is acicular and cataclastic amphibole (Figure 4e; classified as tremolite, see chapter 4.2). Angular to subangular chromite grains hosted within chromitites can reach up to 800 μm (Figure 4f). Interestingly, chromite grains within listwaenitized chromitites appear highly brecciated, almost pulverized (Figure 5a), when compared to the fresh counterparts. Chlorite is developed and partially substitutes chromite around its rims. In places, few talc relics were identified within the listwaenitized chromitites. Carbonate mineral deposition within veins took place in different conditions, as pointed out by their texture, i.e., nodular dusty-beige colored dolomite followed by layered dolomite and thin calcite layers are found in the center of the veins (Figure 4f), and finally, the previous succession is cross-cut by quartz veins.

In general, listwaenitized chromitites are poor in Ni-bearing sulphides and arsenides compared to their unaltered counterparts. The same applies for the platinum group minerals (PGM). The main PGM phases encountered in both studied occurrences are euhedral to subhedral laurite, always entrapped within chromite grains (Figure 5b). Their

small size (<7 μm) oftentimes inhibits their quantitative analysis. Desulfurization of laurite grains within listwaenitized chromitites is aided by fractures along the chromite grains (Figure 5b–d). Magnesites are, in most cases, cryptocrystalline (Figure 5e); however, in places, magnesite recrystallizes. Targeted petrographical study of micro-scale inclusions revealed the presence of halite, sylvite (Figure 5f), and manganese oxides (Figure 5g). Serpentine, chlorite, talc, tremolite, and quartz participate in traces.

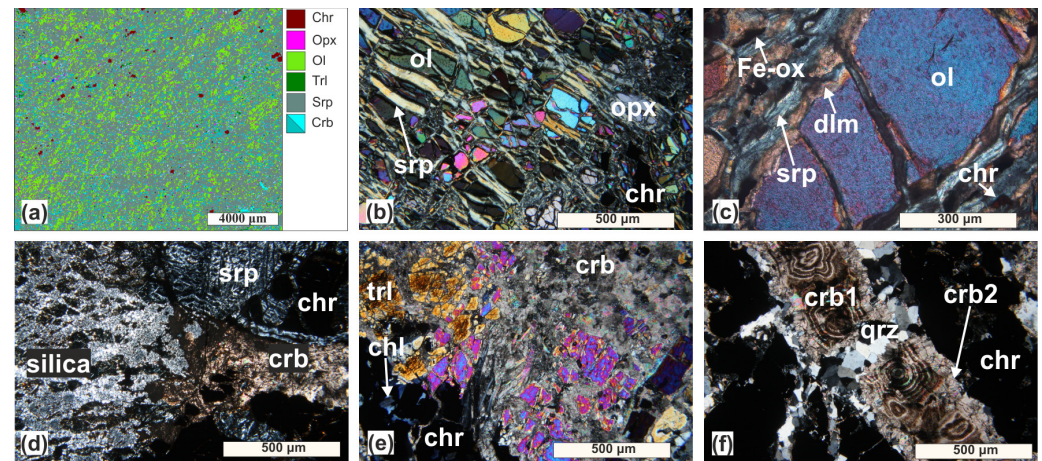


Figure 4. (a) QEMSCAN false-color image illustrating altered cataclastic dunite with olivine being fragmented into $\sim 86 \mu\text{m}$ particles; photomicrographs of: (b) coarse grained cataclastic dunite composed of olivine (up to $500 \mu\text{m}$) that is altered into serpentine; (c) fractured olivine grained altered into dolomite, serpentine and Fe-oxides; (d) listwaenitized chromitite composed of silica mass and relict serpentine patches, carbonate veins and chromite; (e) listwaenitized chromitite consisting of acicular tremolite and granoblastic carbonates and relict chromite with chlorite corona; (f) vein consisting of two carbonate phases, namely nodular and layered, predating quartz's deposition. Abbreviations: chr = chromite; opx = orthopyroxene; ol = olivine; trl = tremolite; srp = serpentine; crb = carbonate minerals; dlm = dolomite; Fe-ox = Fe-oxides; chl = chlorite; qrz = quartz; crb1 and crb2 two petrographically distinct carbonate phases.

4.2. Mineral Chemistry

The mineral phases that have been analyzed via EMPA are chromite, chlorite, and amphibole. Amphibole within the listwaenitized chromitites was further analyzed for its trace elements via LA-ICP-MS. Spinel group mineral grains of the studied listwaenitized chromitites are classified as magnesiochromite, nomenclature after [31], with $\text{Cr}\# = 0.71\text{--}0.78$ [$\text{Cr}/(\text{Cr} + \text{Al})$] and $\text{Mg}\# = 0.44\text{--}0.54$ [$\text{Mg}/(\text{Mg} + \text{Fe}^{2+})$], respectively, whereas Al_2O_3 concentrations range from 9.67 to 14.52 wt% (Table S2). Analyses were conducted in traverses in order to study any chemical variations due to listwaenitization upon their chemistry. A minor depletion in cation proportions of Al^{3+} and Mg^{2+} in analyses proximate to cracks and rims and an increase in Cr^{3+} is noticed, but these differences are rather limited in magnitude (Figure 6a–c, respectively). The aforementioned changes are also depicted in the $\text{Cr}\#$ vs. $\text{Mg}\#$ diagram, whereas analyses near rims/cracks appear enriched in $\text{Cr}\#$ and poor in $\text{Mg}\#$ when compared to the core analyses (Figure 6d). Trace elements in magnesiochromite grains from unaltered and listwaenitized chromitites were also examined. Their MORB-normalized [32] patterns (Figure 6e) are subparallel with negative Ga and Ni anomalies and their difference lies on the positive V anomaly, being noted for the case of listwaenitized hosted magnesiochromite. Moreover, no substantial differences were noted between core and rim analyses of the grains (Table S3).

Amphibole filling chromitite interstices and magnesite veins is classified as tremolite according to [33] [$100 \times \text{Mg}/(\text{Mg} + \text{Fe}^{2+}) > 97.67$; $\text{Si} = 7.81\text{--}7.93$ apfu] (Table S4). Their normalized-to-Chondrite (Ch) patterns appear flat and slightly more enriched than chondrite (Table S5), displaying negative anomalies in Hf and Eu (Figure 7a). When normalized to Primitive Mantle (PM) values, the multi-elemental patterns are characterized by

(a) positive anomalies in Cs, Th-U, Pb, Nd, and Sm, (b) negative anomalies in Rb-Ba, Nb-Ta, Sr-P, Zr, Eu-Ti, and (c) flat, almost mantle level, HREE (Figure 7b). Chlorite (var. penninite after [34]; Si = 6.7–7.0 apfu; Fe²⁺ + Fe³⁺ < 0.14,) is chromian with Cr₂O₃ ranging between 3.3–5.5 wt%, the thermometer of Kranidiotis et al. [35] yielded temperatures ranging between 127–157 °C (Table S6). Selective analyses of carbonate minerals are presented in Table S7.

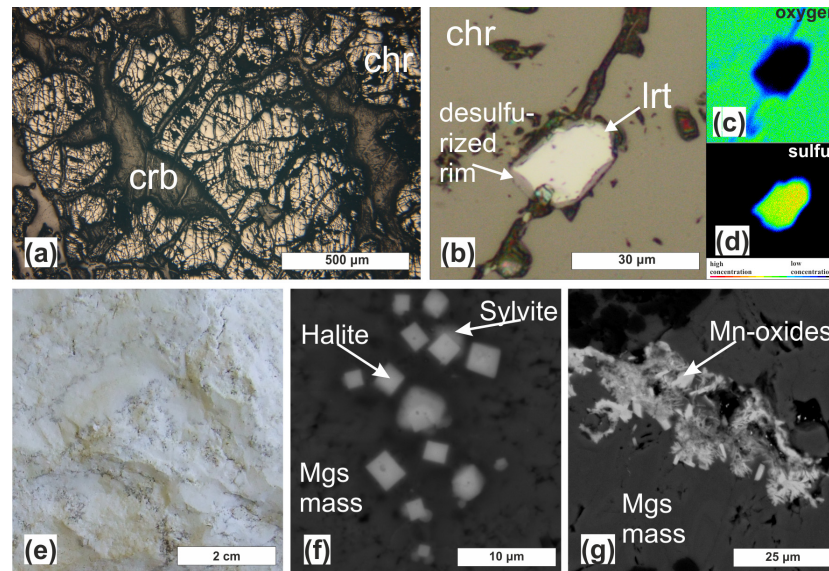


Figure 5. Photomicrographs of: (a) highly brecciated chromitite consisting of chromite and carbonates; (b) desulfurized laurite grain entrapped in chromite; chemical mapping of the desulfurized laurite grain (c) oxygen concentrations; (d) sulfur concentrations, note that sulfur is absent from the desulfurized laurite rim; (e) macroscopic photo of cryptocrystalline magnesite; (f) back-scattered electron image of halite and sylvite grains hosted within magnesite; (g) back-scattered electron image of Mn-oxides hosted within magnesite. Abbreviations: lrt = laurite; Mgs = magnesite; crb = carbonate minerals; chr = chromite.

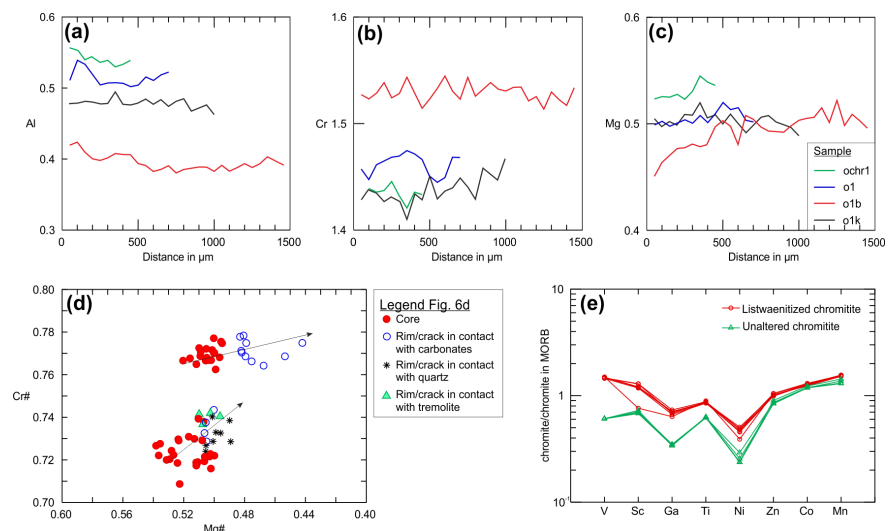


Figure 6. (a–c) compositional variations of cation proportions Al, Cr and Mg, respectively through magnesiochromite grains hosted within listwaenitized chromitites (samples: ochr1; o1; o1b; o1k); (d) Cr# vs. Mg# diagram of the aforementioned grains distinguished into core analyses and analyses adjacent to rims and cracks, arrows represent the alteration of the magnesiochromite grains; (e) normalized [32] LA-ICP-MS trace element patterns of magnesiochromite grains hosted within listwaenitized and unaltered chromitites.

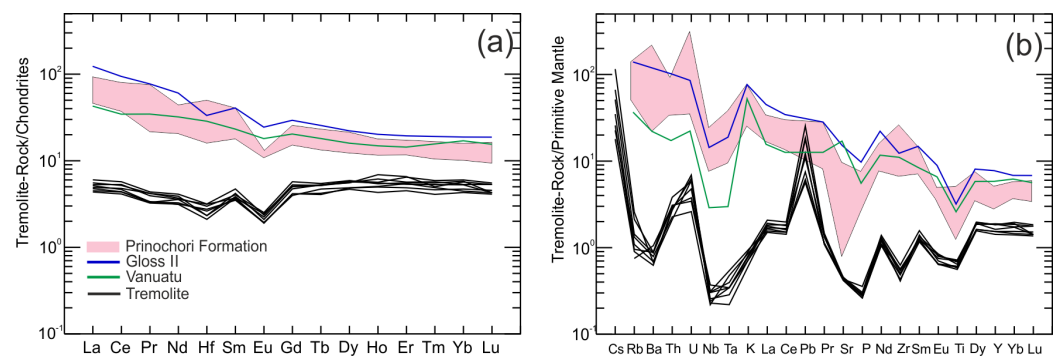


Figure 7. Tremolite (a) Chondrite and (b) multielemental Primitive Mantle normalized spider diagrams, after [36], compared to the metasedimentary rocks of Prinochori Formation as pink field after [26] and subducted sediments from Vanuatu and Gloss II, after [37].

4.3. Geochemistry

Whole-rock analyses were conducted upon magnesite, listwaenites, and their protoliths (partially in Table 1 and all analyzed elements and mineral assemblages in Table S8), and listwaenitized chromitites were analyzed for their PGE contents (Table S9). According to petrographical and geochemical features, the analyzed rocks are classified as protoliths, proto-listwaenite, silica listwaenites, and magnesites.

Protoliths consist of dunite and harzburgite SiO_2 ranges from 40.24 to 44.81 wt% and MgO between 35.89 to 46.01 wt% (Figure 8a). The contents of the aforementioned two oxides can aid the overall classification of the studied rocks. Moreover, protoliths concentrate small amounts wt% of TiO_2 (<0.009 wt%), K_2O (below detection limit), CaO (<0.51 wt%), and Al_2O_3 (<0.63 wt%). The protoliths' REE concentrations are rather depleted, ranging between 0.082–0.845 ppm, demonstrating U-shaped Ch-normalized patterns (Figure 8c).

Serpentinized rocks from this study and other Vardar ophiolite occurrences [38] demonstrate gradual enrichment in SiO_2 and decrease of MgO contents; Iddingsitized serpentine (proto-listwaenite) consists of 38.03 wt% SiO_2 and 25.17 wt% MgO. Fe_2O_3 concentrations are more enriched in dunite and serpentine with high LOI (7.88–18.9 wt%). However, there is a compositional gap between the serpentinites and the listwaenites, with the latter following a different trend (Figure 8a).

Listwaenites are silica rich, and MgO depleted rocks ranging between 80.95–96.34 and 0.37–9.11 wt%, respectively, taking into account previous research [16], the aforementioned concentrations eventually are 69.52–96.34 wt% and 0.37–9.58 wt%, respectively. Listwaenites similar to those reported in this study, i.e., with silica contents > 80 wt% and substantial amounts of red-colored mass (rusty silica, see Chapter 4.1) comprising of Fe-hydroxides and oxides, are classified as silica listwaenites (or birbirites) [7,10]. V/Sc ratios demonstrate an increase with increasing SiO_2 from protoliths and serpentinites towards the listwaenites (Figure 8b); with Sc being removed and V being introduced during listwaenitization. Cr, Co, Ni, and Zn concentrations are also being removed, and an enrichment is noted in Pb, As, Rb, Sr, Cs, and Au contents during listwaenitization (Tables 1 and S8). The serpentinized/carbonatized dunites are generally compositionally comparable with the reported protoliths and even more depleted in ΣREE (Figure 8c). In the PM-normalized diagrams, the serpentinized and carbonatized samples demonstrate positive Cs, Th, and Pb anomalies, characterized by low to below detection limits concentrations of Rb, Ba, Nb, Ta, Zr, and Ti. Listwaenites' ΣREE concentrations range from 0.25 to 2.13 ppm, more elevated than their protoliths, although they retain a U-shape in Ch-normalized REE pattern (with a substantial increase in LREE; Figure 8e) couple with (a) positive Cs, Th, U, Pb, and P and (b) negative Rb, Ba, and Zr anomalies in the PM-normalized patterns (Figure 8f).

Magnesites consist mainly of MgO 41.71–47.06 wt% with small amounts of CaO (0.34–1.77 wt%). They make for the poorest lithology in REE contents < 1.7 ppm (Figure 8e).

Their PM-normalized patterns demonstrate positive Cs, Pb, and negative Rb-Ba anomalies, and low and below-detection limit Ti, Zr, Th, and U concentrations (Figure 8f).

Table 1. Major (wt%) and trace (ppm, Au in ppb) element concentrations of the studied protoliths, proto-listwaenite, silica listwaenites and magnesites from the Vavdos and Gerakini-Ormylia mantle section; “-”: bellow detection.

| Sample | Rock Type | SiO ₂ | Al ₂ O ₃ | Fe ₂ O ₃ | MnO | MgO | CaO | Na ₂ O | K ₂ O | TiO ₂ | P ₂ O ₅ | LOI | Total |
|--------|--|------------------|--------------------------------|--------------------------------|-------|-------|------|-------------------|------------------|------------------|-------------------------------|------|-------|
| B6H | protolith_harzburgite | 44.81 | 0.45 | 8.57 | 0.126 | 43.53 | 0.55 | - | - | 0.004 | - | 0.42 | 98.45 |
| O64 | protolith dunite | 40.61 | 0.47 | 8.36 | 0.12 | 40.71 | 0.41 | 0.02 | - | 0.007 | - | 7.88 | 98.58 |
| O62 | protolith dunite | 43.08 | 0.63 | 7.93 | 0.114 | 46.01 | 0.41 | - | - | 0.009 | - | 1.62 | 99.83 |
| O42 | protolith carbonitized dunite | 40.24 | 0.42 | 11.72 | 0.16 | 35.89 | 0.38 | - | - | - | 0.02 | 9.8 | 99.38 |
| DK3 | iddingsitized serpentinite (proto-listwaenite) | 38.03 | 0.2 | 9.57 | 0.12 | 25.17 | 6.65 | - | - | - | - | 18.9 | 99.55 |
| B94 | silica listwaenite | 94.3 | 0.21 | 2.9 | 0.03 | 0.37 | 0.04 | - | - | - | 0.03 | 1.9 | 99.98 |
| O1 | silica listwaenite | 87.7 | 0.09 | 5.21 | 0.07 | 1.19 | 1.66 | - | - | - | 0.02 | 3.6 | 99.95 |
| O1B | silica listwaenite | 84.54 | 0.17 | 4.91 | 0.065 | 5.35 | 0.99 | - | - | - | 0.02 | 3.79 | 99.84 |
| B83 | silica listwaenite | 80.95 | 0.37 | 4.31 | 0.06 | 9.11 | 0.27 | - | - | - | 0.02 | 4.4 | 99.84 |
| V2 | magnesite | 1.98 | - | 0.07 | - | 41.71 | 0.54 | - | - | - | - | 50.5 | 94.79 |
| V3 | magnesite | 0.3 | - | - | - | 47.06 | 0.42 | - | - | - | - | 51.4 | 99.22 |
| V4 | magnesite | 0.07 | - | - | - | 44.35 | 0.34 | - | - | - | - | 51.3 | 96.08 |
| G-3 | magnesite | 0.09 | - | - | - | 42.65 | 1.77 | - | - | - | - | 50.9 | 95.45 |
| G-4 | magnesite | 1.64 | - | 0.05 | - | 43.13 | 0.46 | - | - | - | - | 50.8 | 96.12 |

| Sample | Sc | V | Cr | Co | Ni | As | Rb | Sr | Pb | Au |
|--------|----|-----|------|-------|-------|-----|-----|------|------|-----|
| B6H | 10 | 32 | 2580 | 111 | 2360 | - | - | - | 5 | - |
| O64 | 8 | 27 | 3090 | 102 | 2130 | - | - | - | - | - |
| O62 | 6 | 27 | 3280 | 117 | 2610 | - | - | - | - | - |
| O42 | 6 | 32 | 3220 | 135.2 | 2164 | - | 0.6 | 8.3 | 3 | 1.1 |
| DK3 | 4 | 25 | 5190 | 116.5 | 1637 | 0.9 | 0.6 | 41.2 | 6.9 | 1.4 |
| B94 | 1 | 77 | 930 | 27.1 | 542 | 3.2 | 0.7 | 1.4 | 7.9 | 5.1 |
| O1 | 2 | 126 | 2130 | 68.7 | 930 | 7.5 | 1.3 | 6.4 | 11.1 | 2.6 |
| O1B | 4 | 103 | 2120 | 61.8 | 989 | 5.7 | 1.1 | 3.9 | 9 | 3.4 |
| B83 | 5 | 83 | 1480 | 56.4 | 1260 | 4.8 | 0.5 | 1.9 | 6 | 3.1 |
| V2 | - | - | - | 1 | 27.8 | - | 0.3 | 2.7 | 2.5 | 3.1 |
| V3 | - | - | - | 0.6 | 409.8 | - | 0.3 | 5.2 | 4.2 | 0.9 |
| V4 | - | - | - | 0.2 | 39.3 | - | - | 2.7 | 5.8 | 1.8 |
| G-3 | - | - | - | - | 351.9 | - | - | 9.7 | 3.8 | - |
| G-4 | - | - | - | 0.5 | 12.6 | - | 0.4 | 3.1 | 1.8 | 0.5 |

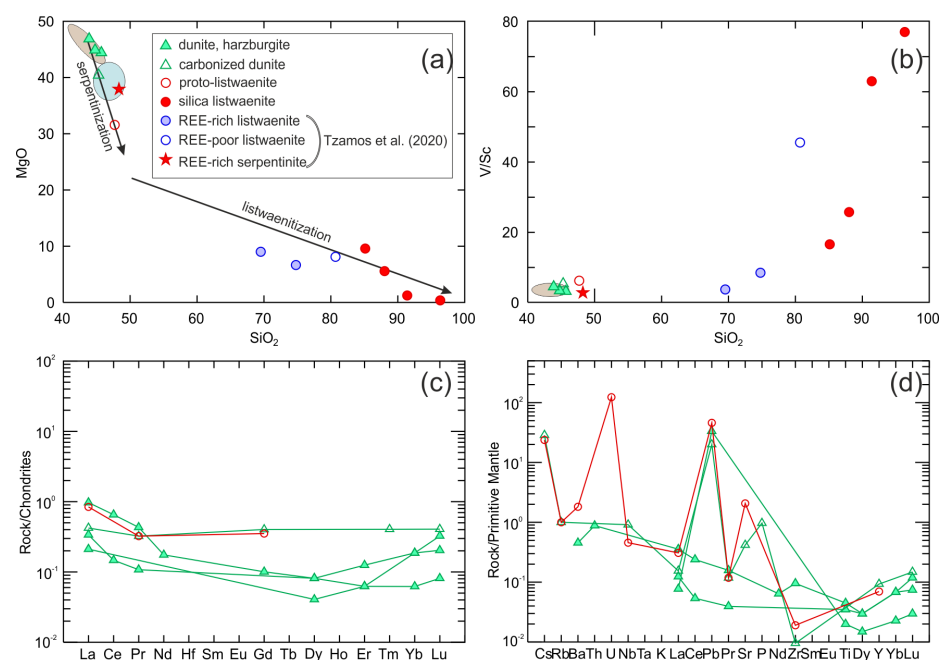


Figure 8. Cont.

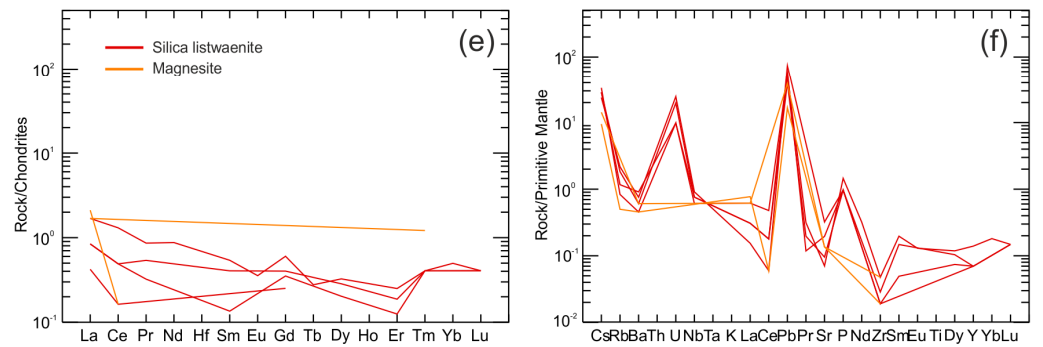


Figure 8. Geochemical diagrams (a) MgO vs. SiO₂; (b) V/Sc vs. SiO₂; (c) Chondrite-normalized REE patterns, after [36], of the studied unaltered and altered peridotites; (d) Primitive mantle-normalized multielemental patterns, after [36], of the studied unaltered and altered peridotites; (e) Chondrite-normalized REE patterns of the studied listwaenites and magnesites; (f) Primitive mantle-normalized multielemental patterns of the studied listwaenites and magnesites. Grey field peridotites reported by [16]; blue field serpentinites from Vardar derive ophiolitic remnants, reported by [38].

Listwaenitized chromitites accumulate 221.0–362.0 ppb of ΣPGE. They are enriched in IPGE over PPGE with low Pd/Ir ratios ranging from 0.20 to 0.67. They present positive Ru anomalies, negative Ru-Pt, and positive Pt-Au scales (Figure 9). Concerning the none listwaenitized chromitites, they concentrate ΣPGE between 132.3–207.8 ppb displaying identical PGE patterns [22]. Pd-Au positive slopes are present in all listwaenite-hosted chromitites and this is not the case for the dunite-hosted chromitites. On average, the listwaenite-hosted chromitites demonstrate higher Pd/Ir ratios (avg. = 0.47) when compared to their non-metasomatized counterparts (avg. = 0.32), higher ΣPGE concentrations of 293 versus 137 ppb, and higher Au 10.7 versus 4.14 ppb. The average compositions presented in Figure 9 only differ in Pd, which demonstrates positive anomaly in the listwaenitized samples and negative in the unaltered samples.

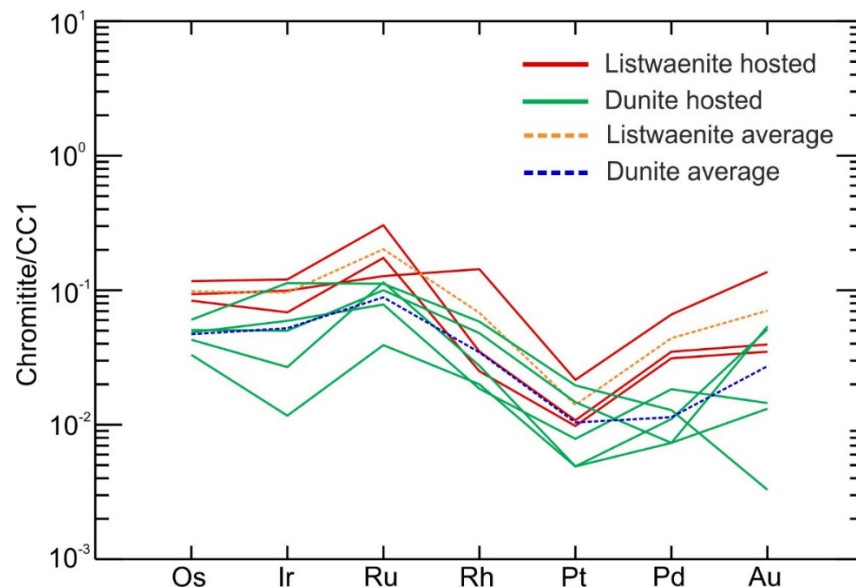


Figure 9. Chondrite-normalized PGE concentrations, after [39], of chromitites hosted within unaltered dunites [22] and listwaenites (reported in this study), the average compositions of each group are also presented.

5. Discussion

5.1. Peridotite Pervasive Listwaenitization into 'Quartzite' and Late-Stage Clay Mineral Genesis—Geochemical Changes

Dunite–chromitite assemblages served as the protolith of the listwaenitized chromitites. It has been proven that chromitite and dunite of the W. Chalkidiki ophiolites were formed through melt–rock interaction between boninitic melts and harzburgite within the forearc region [22]. However, apart from the evidence from the field geology, geochemistry also demonstrates the same information. Both listwaenite and dunite, and even harzburgite, demonstrate U-shaped Ch-normalized patterns typical for mantle rocks interacting with boninitic melts. In the MgO–SiO₂ diagram, there is a clear trend from peridotites to listwaenites, nevertheless, there is a compositional gap described by roughly 50–70 wt% SiO₂ and 10–30 wt% MgO. This gap could have been represented by (a) a rock enriched in talc or (b) a rock composed by variable amounts of serpentine, silica, and carbonates. The first point seems plausible since a 2–3 m talc schist body was found in the base of the listwaenite formation in the Vavdos ophiolite. Moreover, small occurrences of soapstones were encountered within the altered peridotites, however the exact mechanism of their formation is not completely understood. Talc schist, soapstones, and in general, lithologies enriched in talc are pretty common within listwaenitized peridotite portions [40,41].

The mantle peridotites of W. Chalkidiki are mainly composed of olivine and orthopyroxene (up to 15 vol%) with low amounts of chromite (<2 vol%) and clinopyroxene (<1.5 vol%). Olivine and orthopyroxene are the main reactive mineral components. The question is how the silica-rich listwaenites are formed. Although olivine could directly transform into quartz/silica [12], the petrographical study points to the transformation of serpentine into quartz/silica, since serpentine was indeed preserved and olivine was not. Serpentine can transform into quartz with the liberation of MgO and H₂O [1,42]. This transformation is retained in the form of a pseudo-mesh texture, which silica inherited from the serpentine (Figure 4d). In that way, Mg is mixed with CO₂-bearing fluids and forms the magnesite stockwork. No brucite was encountered in any of the metasomatized rocks. In places, primary minerals are transforming in situ into magnesite (orthopyroxene is more susceptible) and dolomite–serpentine–quartz assemblages. Although these events have not contributed to the magnesite stockwork development (since Mg was deposited in situ), they have rather aided development of disseminated magnesite. The complete replacement of primary silicate minerals into serpentine, and lastly into silica/quartz, is depicted by the loss of Cr, Co, Ni, and Zn during listwaenitization; elements mainly hosted within pyroxenes and olivine.

The vein system hosted within peridotites and listwaenite is an indicator of the complex reactions that the rocks have experienced. The petrographic study of the vein system revealed that the carbonate minerals were crystallized prior to quartz deposition (Figure 4f). Magnesite dominates the lower stratigraphical levels, whereas dolomite is enriched in higher levels accompanied by minor amounts of calcite. These complex veins consisting of dolomite and quartz may also be tremolite-bearing (Figure 4e) with traces of serpentine, chlorite, talc, and calcite. Tremolite most probably derives from a serpentine reaction with fluids enriched in calcium and silica [43]. Magnesiochromite develops a penninite corona (Figure 4e). The temperature estimations give a range of 127–157 °C for the chlorite (geothermometer of [35]), but these temperatures represent re-equilibration, since chlorite is produced after chromite in relatively elevated temperatures > 400 °C [44].

Listwaenitized chromitites are highly fractured and this is probably due to hydrofracturing during metasomatism. This enabled the alteration of primary PGM with their subsequent desulfurization, as, according to the scanning images, a small increase of oxygen in the rims was noted, pointing to the substitution of sulfur by oxygen, typical of serpentinization-affected PGM [45,46]; therefore, PGM were most likely modified during the predating serpentinization. Some of the most important geochemical changes during listwaenitization of the primary assemblage of dunite–chromitite is the enrichment of PPGE and Au, processes common during listwaenitization and low-T hydrothermal alteration

conditions [1,15,47]. The chemistry of the magnesiochromite grains is not altered significantly, both in terms of major and trace elements, and the reason for this is the high ratios of magnesiochromite/other mineral phases that, in general, aid in preserving primary features [22]. Hence, the compositions of magnesiochromite grains are pristine and not modified, and the normalized trace element patterns (Figure 6e) are typical of fore-arc boninite-derived chromitites, such as the chromitites of the Thetford mines [32], coinciding with the results of previous research [22,27].

Palygorskite, sepiolite, and smectite are commonly associated with diagenetic minerals and rocks such as dolomite and evaporites [48–50], as well as with hydrothermally altered rocks [51]. The type of newly formed clay mineral is controlled by the activities of Mg^{2+}/H^+ and H_4SiO_4 , as well as the pH values that range between 7.6–8.3, whereas the temperature can reach up to 100 °C [52,53]. The fluids that participate may be of meteoric, groundwater, or seawater origin [52,53]. Smectites are commonly formed due to alteration of mica group minerals [54], which are abundant within the studied dolomite–biotite veins (Figures 2f and 3b). These veins represent the uppermost part of the carbonate vein system. Further alteration led to transformation of smectites into fibrous minerals (Figure 3b), most likely represented by palygorskite [55] (Figure 3c). Sepiolite may have crystallized after reaction between dolomite and H_4SiO_4 [53] (Figure 3d), the latter being produced by SiO_2 dissolution in H_2O and high pH values [56]. Although the aforementioned clay minerals can be directly precipitated from a solution [55,57], we consider the transformation of pre-existing mineral phases more plausible since the clay minerals were only developed surficially upon these pre-existing phases.

5.2. Thermodynamic Modeling of Proto-Listwaenite and Silica-Rich Listwaenite

Thermodynamic P-T conditions for the initial and the final stage of listwaenitization were modeled using the *Perple_X* 6.9.0 [58] software and the internally consistent thermodynamic database of Holland and Powell (2011) [59] in the SFCMAHC (SiO_2 -FeO-CaO-MgO- Al_2O_3 - H_2O - CO_2) system. Calculations of the bulk rock composition were made excluding Na_2O , K_2O , and TiO_2 since their concentrations are negligible and do not affect the mineralogical composition of the studied listwaenite samples. The selected P-T range is 500–5000 bar and ≤ 500 °C respectively and corresponds to common thermodynamic conditions for the development of carbonation processes (290–340 °C and 1–3 kbar; [60]). The state equation of CORK (Compensated-Redlich-Kwong; [61,62]) for H_2O - CO_2 fluids was applied. The following solution models were used: (a) Atg (PN) for serpentine [63], and (b) Ol (HP) for olivine olivine [64]. Chlorite (Chl), calcite (Cal), dolomite (Dol), aragonite (Arag), magnetite (Mag), enstatite (En), quartz (Qtz), diaspore (Dsp), heulandite (Heu), periclase (Prl), and Fe-staurolite (Fst) were considered pure endmembers. In addition, estimations on the vol.% quantities for the distinct mineral phases among the studied listwaenite samples were made using the *PyWerami* software.

The calculated P-T pseudosection for the initial stage of listwaenitization was based on the geochemical and mineralogical composition of the proto-listwaenite sample DK3. This sample mostly includes serpentine + calcite + magnetite + quartz (labelled with blue color; Figure 10a). This mineralogical assemblage is thermodynamically stable at pressures ≤ 1.6 kbar and temperatures between ~ 270 and 340 °C. The stability field of sample DK3 is constrained by the occurrence of olivine and magnetite at higher P-T conditions. Quantitative estimations for the mineralogical composition of sample DK3 yield the following percentages: serpentine = ~ 12 vol.%; quartz = ~ 33 vol.%; calcite = ~ 11 vol.% and magnetite = ~ 44 vol.%.

The P-T pseudosection for the late stage of extensive listwaenitization was constructed based on the geochemical and mineralogical composition of the silica listwaenite sample O1 (Figure 10b). The mineralogical assemblage of this sample, which mostly comprises serpentine + quartz + magnetite, as well as minor dolomite and zeolite (labelled with blue color), is thermodynamically stable at pressures $\leq \sim 1.9$ kbar and temperatures $\leq \sim 40$ °C. The stability field of sample O1 is constrained by the presence of Fe-chlorite at higher P-T conditions, as well

as the crystallization of magnetite at lower P-T conditions. Quantitative estimations for the mineralogical composition of sample O1 yield the following range: serpentine = ~6.5 vol.%; quartz = ~87.5 vol.%; dolomite = ~5 vol.%; heulandite + magnetite ≤ 1 vol.%.

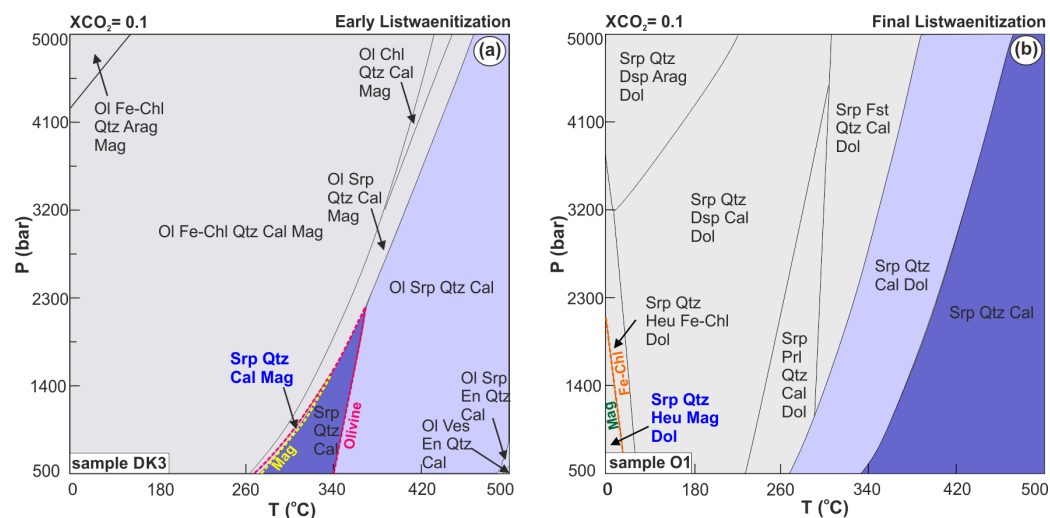


Figure 10. P-T pseudosections on the SFCMAHC ($\text{SiO}_2\text{-FeO-CaO-MgO-Al}_2\text{O}_3\text{-H}_2\text{O-CO}_2$) system for the: (a) initial listwaenitization stage (proto-listwaenite sample DK3) and (b) the final listwaenitization stage (silica-rich listwaenite sample O1).

5.3. Geotectonic Implications and the Role of Subducted Sediments within the Mantle Wedge in Inducing Metasomatism

The studied listwaenites were formed after serpentinized peridotites. Those peridotites formed in the fore-arc region and in SSZ settings of the Vardar ocean, and they represent refractory mantle rocks [22]. In general, serpentinites are distinguished into three main categories, with respect to the geotectonic environment of genesis, (a) abyssal, (b) mantle wedge, and (c) subducted [65]. The trace element geochemistry of the listwaenites, as well as of the serpentinized peridotites (metasomatic rocks) of this study, could aid in confining the geotectonic setting of their evolution. Cs demonstrates great enrichment within altered peridotites, listwaenites, magnesites, and tremolite (PM-normalized diagrams; Figures 7b and 8d,f), and is commonly introduced from a sedimentary source within fore-arc regions [66]. Enrichments in the following elements: Pb, As, Rb, and Sr within the metasomatic rocks (compared to the unaltered counterparts) are also typical of mantle wedge serpentinites [19,65]. The enrichments in Pb and As are attributed to fluids deriving from subducted sediments; carbonate minerals can incorporate Sr and Pb, whereas arsenic is mainly incorporated in serpentine group minerals ([62] and references therein). Hence, the enrichment in all aforementioned elements clearly depicts a mantle wedge environment of serpentinization and subsequent genesis of listwaenites [67,68]. Tremolite is also in agreement with these assumptions since its major element chemistry is typical of continental, rather than oceanic, tectonic environments [69], and trace elements demonstrate similar enrichments (Cs, Pb, Th) with the whole-rock geochemical analyses of listwaenites and magnesites. Interestingly, the normalized patterns of tremolite display similarities with those of other subducted sedimentary sources and the Prinohori formation (Figure 7). The listwaenite formation is controlled by extensional faults [6] aiding the circulation of fluids. Although research points to the participation of meteoric water [14], the presence of halite and sylvite in magnesite point to probable participation of sea water in the system. Isotopic analyses of magnesite further revealed that the carbon is of organic origin [14] and that there is a great affinity with Mesozoic marine sediments of the Vardar zone [70]. Hence, this re-enforces the probability of the Mesozoic Prinohori formation, or any other chemically similar sedimentary formation, to have been subducted beneath

the mantle wedge producing fluids after de-hydration that circulated through the mantle wedge.

6. Conclusions

In the region of W. Chalkidiki ophiolites, listwaenites' protoliths are fore-arc peridotites modified in SSZ settings. More precisely, serpentinization took place in the mantle wedge as inferred by the enrichment in Cs, Pb, As, and V. Loss of Cr, Co, Ni, and Zn is linked with the decomposition of the primary silicates that are their main carriers. Listwaenitized chromitites are enriched in Au and PPGE, and the PGM appear desulfurized, representing serpentinization conditions prior to listwaenitization. Magnesiochromite grains of listwaenitized chromitites demonstrate pristine major and trace element compositions, which is due to the high contents of magnesiochromite versus other mineral phases. Depending on the physicochemical conditions, serpentine has either crystallized into quartz or tremolite, forming listwaenite starting between 270–340 °C and pressure \leq 1.6 kbar. The silica listwaenites are thermodynamically stable at pressures \leq ~1.9 kbar and temperatures \leq ~40 °C. Late-stage clay mineralization is attributed to the alteration of phyllosilicates and dolomite at temperatures $<$ 100 °C. Geochemical results revealed affinities of listwaenites and hosted mineral phases with sedimentary rocks. These sedimentary rocks were subducted, and after de-hydration, produced fluids enriched in CO₂, responsible for the alteration processes within the Vardar Ocean mantle; these are most probably represented by the Mesozoic Princhori Formation.

Supplementary Materials: The following supporting information can be downloaded at: <https://www.mdpi.com/article/10.3390/min12081000/s1>, Table S1: Sample localities and coordinates; Table S2: Successive magnesiochromite analyses conducted in traverses, hosted in listwaenitized chromitites; numbers next to sample name demonstrate the succession that the analyses were conducted; Table S3: LA-ICP-MS analyses (ppm) of magnesiochromite cores and rims hosted in listwaenitized and unaltered chromitite; Table S4: Electron microprobe analyses of tremolite hosted within listwaenitized chromitite; Table S5: LA-ICP-MS analyses of tremolite hosted in listwaenitized chromitite; Table S6: Electron microprobe analyses of chlorite hosted within listwaenitized chromitite; Temperatures were calculated using the geothermometer of Kranidiotis et al., 1987; Table S7: Carbonate mineral analyses (dolomite and calcite) hosted within listwaenitized chromitites; Table S8: Whole-rock geochemical analyses of protoliths, listwaenites, and magnesites along with their mineral assemblages; Table S9: PGE concentrations of listwaenitized chromitites (in ppb).

Author Contributions: Conceptualization, A.S., P.K., B.T., P.T. and K.H.; methodology, A.S., P.K., B.T., P.T., D.P. (Dimitrios Papoulis) and K.H.; software, C.K.; investigation, A.S., C.H., V.S. and D.P. (Dimitrios Papoulis); resources, A.S., P.T., C.H. and F.Z.; data curation, A.S., C.K., C.H., F.Z., C.V.L., D.P. (Dionisios Panagiotaras) and D.P. (Dimitrios Papoulis); writing—original draft preparation, A.S., C.K. and C.V.L.; writing—review and editing, A.S., P.K., B.T., C.H., F.Z., V.S., D.P. (Dionisios Panagiotaras), D.P. (Dimitrios Papoulis) and K.H.; visualization, A.S., C.K. and C.V.L.; supervision, A.S., P.K., B.T. and K.H.; project administration, A.S., P.K., B.T. and K.H.; funding acquisition, A.S. All authors have read and agreed to the published version of the manuscript.

Funding: This research was funded by the Hellenic Foundation for Research and Innovation (HFRI) under the HFRI PhD Fellowship grant (Fellowship Number: 1616).

Data Availability Statement: All data are presented in the Supplementary file.

Acknowledgments: The University Centrum for Applied Geosciences (UCAG) is thanked for the access to the Eugen F. Stumpfl electron microprobe Laboratory. Erasmus + for traineeships is likewise thanked since it provided the opportunity to A. Sideridis to perform analyses in the Eugen F. Stumpfl electron microprobe Laboratory and the LA-ICP-MS system in the NAWI Graz Central Lab for Water, Minerals and Rocks. Tassos Gramatikopoulos and the SGS Mineral Services, Canada are thanked for the QEMSCAN analyses.

Conflicts of Interest: The authors declare no conflict of interest.

References

1. Tsikouras, B.; Karipi, S.; Grammatikopoulos, T.A.; Hatzipanagiotou, K. Listwaenite evolution in the ophiolite mélange of Iti Mountain (continental Central Greece). *Eur. J. Mineral.* **2006**, *18*, 243–255. [\[CrossRef\]](#)
2. Arai, S.; Okamura, H.; Kadoshima, K.; Tanaka, C.; Suzuki, K.; Ishimaru, S. Chemical characteristics of chromian spinel in plutonic rocks: Implications for deep magma processes and discrimination of tectonic setting. *Isl. Arc.* **2011**, *20*, 125–137. [\[CrossRef\]](#)
3. Austrheim, H.; Corfu, F.; Renggli, C.J. From peridotite to fuchsite bearing quartzite via carbonation and weathering: With implications for the Pb budget of continental crust. *Contrib. Miner. Petrol.* **2021**, *176*, 94. [\[CrossRef\]](#)
4. Boskabadi, A.; Pitcairn, I.K.; Leybourne, M.I.; Teagle, D.A.H.; Cooper, M.J.; Hadizadeh, H.; Nasiri Bezenjani, R.; Monazzami Bagherzadeh, R. Carbonation of ophiolitic ultramafic rocks: Listvenite formation in the Late Cretaceous ophiolites of eastern Iran. *Lithos* **2020**, 352–353, 105307. [\[CrossRef\]](#)
5. Menzel, M.D.; Urai, J.L.; de Obeso, J.C.; Kotowski, A.; Manning, C.E.; Kelemen, P.B.; Kettermann, M.; Jesus, A.P.; Harigane, Y. Brittle Deformation of Carbonated Peridotite—Insights From Listvenites of the Samail Ophiolite (Oman Drilling Project Hole BT1B). *J. Geophys. Res. Solid Earth* **2020**, *125*, e2020JB020199. [\[CrossRef\]](#)
6. Mattern, F.; Scharf, A. Postobductional extension along and within the Frontal Range of the Eastern Oman Mountains. *J. Asian Earth Sci.* **2018**, *154*, 369–385. [\[CrossRef\]](#)
7. Moctar, D.O.; Moukadiri, A.; Boushaba, A.; Lemine, S.O.M.; Dubois, M. Petrographical and Geochemical Characteristics of the Mauritanides Belts' Birbrites. In *Conference of the Arabian Journal of Geosciences*; Springer: Berlin/Heidelberg, Germany, 2019; pp. 55–57.
8. Menzel, M.D.; Garrido, C.J.; López Sánchez-Vizcaíno, V.; Marchesi, C.; Hidas, K.; Escayola, M.P.; Delgado Huertas, A. Carbonation of mantle peridotite by CO₂-rich fluids: The formation of listvenites in the Advocate ophiolite complex (Newfoundland, Canada). *Lithos* **2018**, *323*, 238–261. [\[CrossRef\]](#)
9. Peuble, S.; Andreani, M.; Gouze, P.; Pollet-Villard, M.; Reynard, B.; Van de Moortele, B. Multi-scale characterization of the incipient carbonation of peridotite. *Chem. Geol.* **2018**, *476*, 150–160. [\[CrossRef\]](#)
10. Boskabadi, A.; Pitcairn, I.K.; Broman, C.; Boyce, A.; Teagle, D.A.H.; Cooper, M.J.; Azer, M.K.; Stern, R.J.; Mohamed, F.H.; Majka, J. Carbonate alteration of ophiolitic rocks in the Arabian–Nubian Shield of Egypt: Sources and compositions of the carbonating fluid and implications for the formation of Au deposits. *Int. Geol. Rev.* **2017**, *59*, 391–419. [\[CrossRef\]](#)
11. Abu-Jaber, N.S.; Kimberley, M.M. Origin of ultramafic-hosted vein magnesite deposits. *Ore Geol. Rev.* **1992**, *7*, 155–191. [\[CrossRef\]](#)
12. Kelemen, P.B.; Matter, J.; Streit, E.E.; Rudge, J.F.; Curry, W.B.; Blusztajn, J. Rates and mechanisms of mineral carbonation in peridotite: Natural processes and recipes for enhanced, in situ CO₂ capture and storage. *Annu. Rev. Earth Planet. Sci.* **2011**, *39*, 545–576. [\[CrossRef\]](#)
13. Pohl, W. Genesis of magnesite deposits—models and trends. *Geol. Rundsch.* **1990**, *79*, 291–299. [\[CrossRef\]](#)
14. Gartzos, E. Comparative stable isotopes study of the magnesite deposits of Greece. *Bull. Geol. Soc. Greece* **2004**, *36*, 196. [\[CrossRef\]](#)
15. Emam, A.; Zoheir, B. Au and Cr mobilization through metasomatism: Microchemical evidence from ore-bearing listvenite, South Eastern Desert of Egypt. *J. Geochem. Explor.* **2013**, *125*, 34–45. [\[CrossRef\]](#)
16. Tzamos, E.; Bussolesi, M.; Grieco, G.; Maescotti, P.; Crispini, L.; Kasinos, A.; Storni, N.; Simeonidis, K.; Zouboulis, A. Mineralogy and geochemistry of ultramafic rocks from rachoni magnesite mine, Gerakini (Chalkidiki, Northern Greece). *Minerals* **2020**, *10*, 934. [\[CrossRef\]](#)
17. Tarkian, M.; Naidenova, E.; Zhelyaskova-Panayotova, M. Platinum-group minerals in chromitites from the Eastern Rhodope ultramafic complex, Bulgaria. *Miner. Petrol.* **1991**, *44*, 73–87. [\[CrossRef\]](#)
18. Koutsovitis, P. High-pressure subduction-related serpentinites and metarodingites from East Thessaly (Greece): Implications for their metamorphic, geochemical and geodynamic evolution in the Hellenic–Dinaric ophiolite context. *Lithos* **2017**, *276*, 122–145. [\[CrossRef\]](#)
19. Deschamps, F.; Guillot, S.; Godard, M.; Andreani, M.; Hattori, K. Serpentinites act as sponges for fluid-mobile elements in abyssal and subduction zone environments. *Terra Nov.* **2011**, *23*, 171–178. [\[CrossRef\]](#)
20. Ismail, S.A.; Koshnaw, R.I.; Barber, D.E.; Humadi, H.A.; Stockli, D.F. Generation and exhumation of granitoid intrusions in the Penjween ophiolite complex, NW Zagros of the Kurdistan region of Iraq: Implications for the geodynamic evolution of the Arabian-Eurasian collision zone. *Lithos* **2020**, *376*, 105714. [\[CrossRef\]](#)
21. Al Humadi, H.; Väisänen, M.; Ismail, S.A.; Lehtonen, M.; Johanson, B. Subducted basalts and sediments as sources for felsic dykes in the mawat ophiolite, NE Iraq. *Ophioliti* **2021**, *46*, 27–41. [\[CrossRef\]](#)
22. Sideridis, A.; Zaccarini, F.; Koutsovitis, P.; Grammatikopoulos, T.; Tsikouras, B.; Garuti, G.; Hatzipanagiotou, K. Chromitites from the Vavdos ophiolite (Chalkidiki, Greece): Petrogenesis and geotectonic settings; constrains from spinel, olivine composition, PGE mineralogy and geochemistry. *Ore Geol. Rev.* **2021**, *137*, 104289. [\[CrossRef\]](#)
23. Giamas, V.; Koutsovitis, P.; Sideridis, A.; Turberg, P.; Grammatikopoulos, T.A.; Petrounias, P.; Giannakopoulou, P.P.; Koukouzas, N.; Hatzipanagiotou, K. Effectiveness of X-ray micro-CT applications upon mafic and ultramafic ophiolitic rocks. *Micron* **2022**, *158*, 103292. [\[CrossRef\]](#) [\[PubMed\]](#)
24. Kauffmann, G.; Kockel, F.; Mollat, H. Notes on the stratigraphic and paleogeographic position of the Svoula Formation in the innermost zone of the Hellenides (northern Greece). *Bull. la Société Géologique Fr.* **1976**, *S7-XVIII*, 225–230. [\[CrossRef\]](#)
25. Meinhold, G.; Kostopoulos, D.K. The Circum-Rhodope Belt, northern Greece: Age, provenance, and tectonic setting. *Tectonophysics* **2013**, *595*, 55–68. [\[CrossRef\]](#)

26. Meinhold, G.; Kostopoulos, D.; Reischmann, T.; Frei, D.; BouDagher-Fadel, M.K. Geochemistry, provenance and stratigraphic age of metasedimentary rocks from the eastern Vardar suture zone, northern Greece. *Palaeogeogr. Palaeoclimatol. Palaeoecol.* **2009**, *277*, 199–225. [[CrossRef](#)]
27. Sideridis, A.; Zaccarini, F.; Grammatikopoulos, T.; Tsitsanis, P.; Tsikouras, B.; Pushkarev, E.; Garuti, G.; Hatzipanagiotou, K. First occurrences of ni-phosphides in chromitites from the ophiolite complexes of alapaevsk, Russia and gerakini-ormylia, Greece. *Ofoliti* **2018**, *43*, 75–84. [[CrossRef](#)]
28. Bonev, N.; Marchev, P.; Moritz, R.; Filipov, P. Timing of igneous accretion, composition, and temporal relation of the Kassandra–Sithonia rift-spreading center within the eastern Vardar suture zone, Northern Greece: Insights into Jurassic arc/back-arc systems evolution at the Eurasian plate margin. *Int. J. Earth Sci.* **2015**, *104*, 1837–1864. [[CrossRef](#)]
29. Jochum, K.P.; Nohl, U.; Rothbarth, N.; Schwager, B.; Stoll, B.; Weis, U. Geostandards and Geoanalytical Research Bibliographic Review 2011. *Geostand. Geoanalytical Res.* **2012**, *36*, 415–419. [[CrossRef](#)]
30. Dias, N.M.P.; Gonçalves, D.; Leite, W.C.; Brinatti, A.M.; Saab, S.C.; Pires, L.F. Morphological characterization of soil clay fraction in nanometric scale. *Powder Technol.* **2013**, *241*, 36–42. [[CrossRef](#)]
31. Bosi, F.; Biagioni, C.; Pasero, M. Nomenclature and classification of the spinel supergroup. *Eur. J. Miner.* **2019**, *31*, 183–192. [[CrossRef](#)]
32. Pagé, P.; Barnes, S.-J. Using trace elements in chromites to constrain the origin of podiform chromitites in the Thetford Mines Ophiolite, Québec, Canada. *Econ. Geol.* **2009**, *104*, 997–1018. [[CrossRef](#)]
33. Leake, B.E.; Woolley, A.R.; Arps, C.E.S.; Birch, W.D.; Gilbert, M.C.; Grice, J.D.; Hawthorne, F.C.; Kato, A.; Kisch, H.J.; Krivovichev, V.G.; et al. Nomenclature of amphiboles: Report of the subcommittee on amphiboles of the international mineralogical association commission on new minerals and mineral names. *Miner. Mag.* **1997**, *61*, 295–321. [[CrossRef](#)]
34. Hey, M.H. A new review of the chlorites. *Minerl. Mag. J. Miner. Soc.* **1954**, *30*, 277–292. [[CrossRef](#)]
35. Kranidiotis, P.; MacLean, W.H. Systematics of chlorite alteration at the Phelps Dodge massive sulfide deposit, Matagami, Quebec. *Econ. Geol.* **1987**, *82*, 1898–1911. [[CrossRef](#)]
36. Sun, S.-S.; McDonough, W.F. *Chemical and Isotopic Systematics of Oceanic Basalts: Implications for Mantle Composition and Processes*; Geological Society: London, UK, 1989; Volume 42, pp. 313–345.
37. Plank, T. *The Chemical Composition of Subducting Sediments*; Elsevier: Amsterdam, The Netherlands, 2013; Volume 4, ISBN 9780080983004.
38. Petrounias, P.; Giannakopoulou, P.P.; Rogkala, A.; Sideridis, A.; Koutsovitis, P.; Lampropoulou, P.; Koukouzas, N.; Pomonis, P.; Hatzipanagiotou, K. Influence of Petrogenesis on the Engineering Properties of Ultramafic Aggregates and on Their Suitability in Concrete. *Appl. Sci.* **2022**, *12*, 3990. [[CrossRef](#)]
39. Naldrett, A.J.; Duke, J.M. Platinum metals in magmatic sulfide ores. *Science* **1980**, *208*, 1417–1424. [[CrossRef](#)]
40. Qiu, T.; Zhu, Y. Chromian spinels in highly altered ultramafic rocks from the Sartohay ophiolitic mélange, Xinjiang, NW China. *J. Asian Earth Sci.* **2018**, *159*, 155–184. [[CrossRef](#)]
41. Schwarzenbach, E.M.; Vogel, M.; Fruüh-Green, G.L.; Boschi, C. Serpentinization, Carbonation, and Metasomatism of Ultramafic Sequences in the Northern Apennine Ophiolite (NW Italy). *J. Geophys. Res. Solid Earth* **2021**, *126*, e2020JB020619. [[CrossRef](#)]
42. Power, I.M.; Wilson, S.A.; Dipple, G.M. Serpentinite Carbonation for CO₂ Sequestration. *Elements* **2013**, *9*, 115–121. [[CrossRef](#)]
43. Frost, R.B.; Beard, J.S. On silica activity and serpentinization. *J. Petrol.* **2007**, *48*, 1351–1368. [[CrossRef](#)]
44. Kimball, K.L. Effects of hydrothermal alteration on the compositions of chromian spinels. *Contrib. Miner. Petrol.* **1990**, *105*, 337–346. [[CrossRef](#)]
45. Uysal, I.; Zaccarini, F.; Sadiklar, M.B.B.; Garuti, G. Occurrence of rare Ru-Fe-Os-Ir-oxide and associated Platinum-group minerals (PGM) in the chromitite of Mugla ophiolite, SW-Turkey. *Neues Jahrb. Miner. (Abhandlungen)* **2009**, *185*, 323–333. [[CrossRef](#)]
46. Grieco, G.; Bussolesi, M.; Eslami, A.; Gentile, A.; Cavallo, A.; Lian, D.; Yang, J.; Ghaseminejad, F. Differential platinum group elements (PGE) re-mobilization at low fS₂ in Abdasht and Soghan mafic-ultramafic complexes (Southern Iran). *Lithos* **2020**, *366*, 105523. [[CrossRef](#)]
47. Farré-de-Pablo, J.; Proenza, J.A.; González-Jiménez, J.M.; Aiglsperger, T.; Torró, L.; Domènech, C.; Garcia-Casco, A. Low-temperature hydrothermal Pt mineralization in uvarovite-bearing ophiolitic chromitites from the Dominican Republic. *Miner. Depos.* **2021**, *57*, 955–976. [[CrossRef](#)]
48. Daoudi, L. Palygorskite in the uppermost Cretaceous–Eocene rocks from Marrakech High Atlas, Morocco. *J. Afr. Earth Sci.* **2004**, *39*, 353–358. [[CrossRef](#)]
49. Kadır, S.; Erkoyun, H.; Eren, M.; Huggett, J.; Önalgil, N. Mineralogy, Geochemistry, and Genesis of Sepiolite and Palygorskite in Neogene Lacustrine Sediments Eskişehir Province, West Central Anatolia, Turkey. *Clays Clay Miner.* **2016**, *64*, 145–166. [[CrossRef](#)]
50. Rasooli, N.; Farpoor, M.H.; Mahmoodabadi, M.; Esfandiarpour Boroujeni, I. Genesis and distribution of different mineral assemblages controlled by environmental factors in soils and evaporitic deposits of Lut Desert, central Iran. *Environ. Earth Sci.* **2021**, *80*, 779. [[CrossRef](#)]
51. Inoue, A. Formation of Clay Minerals in Hydrothermal Environments. In *Origin and Mineralogy of Clays*; Springer: Berlin/Heidelberg, Germany, 1995; pp. 268–329.
52. Bonatti, E.; Craig Simmons, E.; Breger, D.; Hamlyn, P.R.; Lawrence, J. Ultramafic rock/seawater interaction in the oceanic crust: Mg-silicate (sepiolite) deposit from the Indian Ocean floor. *Earth Planet. Sci. Lett.* **1983**, *62*, 229–238. [[CrossRef](#)]

53. Yalçın, H.; Bozkaya, Ö. Ultramafic-Rock-Hosted Vein Sepiolite Occurrences in the Ankara Ophiolitic Mélange, Central Anatolia, Turkey. *Clays Clay Miner.* **2004**, *52*, 227–239. [[CrossRef](#)]
54. Ekinçi Şans, B.; Esenl, F.; Kadir, S.; Elliott, W.C. Genesis of smectite in siliciclastics and pyroclastics of the Eocene İslambeyli Formation in the Lalapaşa region, NW Thrace, Turkey. *Clay Miner.* **2015**, *50*, 459–483. [[CrossRef](#)]
55. Jamoussi, F.; Ben Aboud, A.; López-Galindo, A. Palygorskite genesis through silicate transformation in Tunisian continental Eocene deposits. *Clay Miner.* **2003**, *38*, 187–199. [[CrossRef](#)]
56. Brownlow, A. *Geochemistry*, 2nd ed.; Prentice Hall: Hoboken, NJ, USA, 1995.
57. Karakaya, M.Ç.; Karakaya, N.; Temel, A. Mineralogical and geochemical characteristics and genesis of the sepiolite deposits at Polatlı Basin (Ankara, Turkey). *Clays Clay Miner.* **2011**, *59*, 286–314. [[CrossRef](#)]
58. Connolly, J.A.D. The geodynamic equation of state: What and how. *Geochem. Geophys. Geosystems* **2009**, *10*, n/a-n/a. [[CrossRef](#)]
59. HOLLAND, T.J.B.; POWELL, R. An improved and extended internally consistent thermodynamic dataset for phases of petrological interest, involving a new equation of state for solids. *J. Metamorph. Geol.* **2011**, *29*, 333–383. [[CrossRef](#)]
60. Pirajno, F. Effects of metasomatism on mineral systems and their host rocks: Alkali metasomatism, skarns, greisens, tourmalinites, rodingites, black-wall alteration and listvenites. In *Metasomatism and the Chemical Transformation of Rock*; Springer: Berlin/Heidelberg, Germany, 2013.
61. Holland, T.; Powell, R. A Compensated-Redlich-Kwong (CORK) equation for volumes and fugacities of CO₂ and H₂O in the range 1 bar to 50 kbar and 100–1600 °C. *Contrib. Mineral. Petrol.* **1991**, *109*, 265–273. [[CrossRef](#)]
62. HOLLAND, T.J.B.; POWELL, R. An internally consistent thermodynamic data set for phases of petrological interest. *J. Metamorph. Geol.* **2004**, *16*, 309–343. [[CrossRef](#)]
63. Padrón-Navarta, J.A.; Sánchez-Vizcaíno, V.L.; Hermann, J.; Connolly, J.A.D.; Garrido, C.J.; Gómez-Pugnaire, M.T.; Marchesi, C. Tschermak's substitution in antigorite and consequences for phase relations and water liberation in high-grade serpentinites. *Lithos* **2013**, *178*, 186–196. [[CrossRef](#)]
64. Holland, T.; Powell, R. Thermodynamics of order-disorder in minerals; II, Symmetric formalism applied to solid solutions. *Am. Miner.* **1996**, *81*, 1425–1437. [[CrossRef](#)]
65. Deschamps, F.; Godard, M.; Guillot, S.; Hattori, K. Geochemistry of subduction zone serpentinites: A review. *Lithos* **2013**, *178*, 96–127. [[CrossRef](#)]
66. Peters, D.; Bretscher, A.; John, T.; Scambelluri, M.; Pettke, T. Fluid-mobile elements in serpentinites: Constraints on serpentinitisation environments and element cycling in subduction zones. *Chem. Geol.* **2017**, *466*, 654–666. [[CrossRef](#)]
67. Hamdy, M.M.; Lasheen, E.S.R.; Abdelwahab, W. Gold-bearing listwaenites in ophiolitic ultramafics from the Eastern Desert of Egypt: Subduction zone-related alteration of Neoproterozoic mantle? *J. Afr. Earth Sci.* **2022**, *193*, 104574. [[CrossRef](#)]
68. Kelemen, P.B.; Carlos de Obeso, J.; Leong, J.A.; Godard, M.; Okazaki, K.; Kotowski, A.J.; Manning, C.E.; Ellison, E.T.; Menzel, M.D.; Urai, J.L.; et al. Listvenite Formation During Mass Transfer into the Leading Edge of the Mantle Wedge: Initial Results from Oman Drilling Project Hole BT1B. *J. Geophys. Res. Solid Earth* **2022**, *127*, e2021JB022352. [[CrossRef](#)]
69. Di Giuseppe, D.; Perchiazzi, N.; Brunelli, D.; Giovanardi, T.; Nodari, L.; Della Ventura, G.; Malferrari, D.; Maia, M.; Gualtieri, A.F. Occurrence and characterization of tremolite asbestos from the Mid Atlantic Ridge. *Sci. Rep.* **2021**, *11*, 6285. [[CrossRef](#)] [[PubMed](#)]
70. Dabitzias, S.G. Petrology and genesis of the vavdos cryptocrystalline magnesite deposits, chalkidiki peninsula, Northern Greece. *Econ. Geol.* **1980**, *75*, 1138–1151. [[CrossRef](#)]